Strain-induced electronic and magnetic transition in the $S = \frac{3}{2}$ antiferromagnetic spin chain compound LaCrS$_3$

Kuldeep Kargeti, Aadit Sen, and S. K. Panda[*]

Department of Physics, Bennett University, Greater Noida 201310, Uttar Pradesh, India

Exploring the physics of low-dimensional spin systems and their pressure-driven electronic and magnetic transitions is a thriving research field in modern condensed matter physics. In this context, recently antiferromagnetic Cr-based compounds such as CrI$_3$, CrBr$_3$, and CrGeTe$_3$ have been investigated experimentally and theoretically for their possible spintronics applications. Motivated by the fundamental and industrial importance of these materials, we theoretically studied the electronic and magnetic properties of a relatively less explored Cr-based chalcogenide, namely LaCrS$_3$, where two-dimensional (2D) layers of magnetic Cr^{3+} ions form a rectangular lattice. We employed density functional theory + Hubbard U approach in conjunction with constrained random-phase approximation, where the latter was used to estimate the strength of U. Our findings at ambient pressure show that the system exhibits a semiconducting antiferromagnetic ground state with a gap of 0.5 eV and large Cr moments that correspond to a nominal $S = 3/2$ spin state. The first nearest neighbor (NN) interatomic exchange coupling (J_1) is found to be strongly antiferromagnetic, while the second NN couplings are relatively weaker ferromagnetic (FM), making this system a candidate for a 1D nonfrustrated antiferromagnetic spin-chain family of materials. Based on orbital resolved interactions, we demonstrated the reason behind two different types of interactions among first and second NNs despite their very similar bond lengths. We observe a significant spin-orbit coupling effect, giving rise to a finite magnetocrystalline anisotropy, and Dzyaloshinskii-Moriya interaction. Further, we found that by applying uniaxial tensile strain along the crystallographic a and b axis, LaCrS$_3$ exhibits a magnetic transition to a semiconducting FM ground state, while compression gives rise to the realization of a gapless semiconducting antiferromagnetic ground state. Thus our findings can enrich the versatility of LaCrS$_3$ and make it a promising candidate for industrial applications.

I. INTRODUCTION

The electronic structure and magnetism of one-dimensional (1D) spin chain systems is a thriving research field in modern condensed matter physics [1] as they are used for the analyses of many fundamental concepts in many-body quantum physics as well as have great technological promises for quantum computation and information processing. The quantum spin fluctuations are an intrinsic characteristic of such low-dimensional magnetic systems having localized spin moments. These fluctuations, the rich electron correlated behavior, and spin-orbit coupling often lead to emergent phenomena such as Haldane gap states [2,3] and new topological phases of matter [4]. In this direction, the Cr-based semiconducting materials with layered structures have recently obtained substantial attention due to their potential application for many technologies from sensing to data storage. For instance, the experimental demonstration of long range magnetism in layered materials, e.g., Cr trihalides (CrX$_3$, X = I, Br, and Cl), is considered as a major breakthrough in the field of low dimensional magnetism since it opens up opportunities for sprintronics applications [5]. There are also reports of strain-based tuning of magnetism

in layered materials such as CrGeTe$_3$ which has emerged as an excellent magnetic substrate in nanoelectronic devices and also for next-generation memory devices [6].

In view of the fact that layered Cr-based materials have huge fundamental and industrial importance, we theoretically studied the electronic and magnetic properties of a relatively less explored Cr-based chalcogenide, namely LaCrS$_3$. The crystal structure of LaCrS$_3$ is displayed in Fig. 1(a) where 2D layers of magnetic Cr^{3+} ions form a rectangular lattice. The edge sharing CrS$_6$ unit forms a double chain along the b direction and each Cr is connected to the other two Cr ions via S ions as illustrated in Fig. 1(b). The Cr-Cr distances in the triangles of this double chain are 3.47 Å (Cr$_1$-Cr$_2$ and Cr$_2$-Cr$_3$) and 3.83 Å (Cr$_1$-Cr$_3$), respectively, and the interchain Cr-Cr distance in the ab plane [the third nearest neighbor: Cr$_2$-Cr$_2$ in Fig. 1(a)] is 5.83 Å. The Cr-S bond distances of CrS$_6$ octahedra lie in the range between 2.38 Å and 2.48 Å. The experimental resistivity data [7] indicates that the ground state is insulating. The magnetic susceptibility (χ) [7] increases with decreasing temperature and passes through a broad maximum at around 195 K, which is a typical feature of short-range spin correlation [8]. The high-temperature fitting of χ gives the Weiss temperature as -8.5 K, indicating antiferromagnetic coupling between the Cr ions. At lower temperatures well below the broad maximum, the χ decays exponentially which could be attributed to the opening of a spin gap.
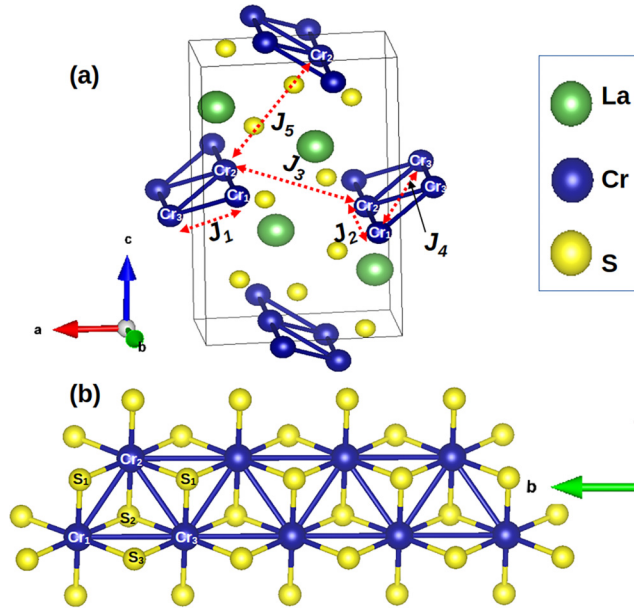
*swarup.panda@bennett.edu.in

FIG. 1. (a) Unit cell of LaCrS$_3$. The magnetic couplings between nearest neighbor Cr ions are marked. (b) The CrS$_6$ edge-sharing octahedral units form the zigzag chain running along the b axis.
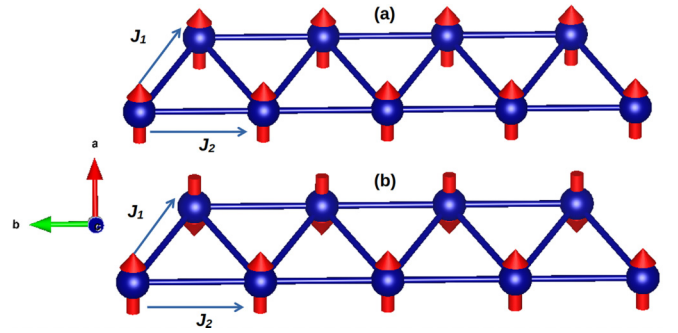

FIG. 2. (a) Ferromagnetic ordering and (b) antiferromagnetic ordering between the nearest neighbor Cr ions. These two magnetic configurations are considered to get the lowest energy state.

The microscopic understanding of the magnetism of LaCrS$_3$, particularly to find out if it belongs to the family of spin-chain compounds, requires a detailed knowledge of the magnetic spin Hamiltonian. Such understanding will also help us to predict the efficient ways of tuning its spin interactions, magnetic, electronic phases, and emergence of magnetic phenomena [9], which are important for technological and scientific aspects. The tuning of the various properties such as modification of interatomic exchange couplings, magnetic anisotropies, critical magnetic transition temperature, band-gap tuning, etc., are possible under the influence of mechanical strain. We present here theoretical calculations to comprehend the electronic structure and magnetism of this intriguing correlated material that belongs to the transition metal chalcogenide family.

In this work, we have investigated the electronic and magnetic properties of LaCrS$_3$ using density functional theory + Hubbard U method under ambient conditions and also observed how its properties could be tuned under the influence of compressive and tensile uniaxial strain. Our results show that the first nearest neighbor (NN) and second NN spin interaction strengths between Cr ions are crucially different despite their very similar bond length. In fact, first NN interactions are strong antiferromagnetic, while second NN interactions are relatively weaker ferromagnetic (FM), making this system a 1D nonfrustrated antiferromagnetic $S = 3/2$ spin-chain compound at ambient conditions. We found non-negligible spin-orbit coupling effects, giving rise to a finite MAE, and Dzyaloshinskii-Moriya (DM) interactions. Further, we proposed ways to realize magnetic transition [antiferromagnetic (AFM) to FM], normal semiconductor to a gapless semiconductor transition via application of uniaxial strain.

II. COMPUTATIONAL DETAILS

All calculations reported in this work are carried out using three approaches, namely (a) a plane-wave basis as implemented in Vienna *ab initio* simulation package (VASP) [10,11] with projector augmented wave potentials [12], (b) the full potential linearized augmented plane wave (FP-LAPW) basis as implemented in WIEN2K code [13], and the full-potential linear muffin-tin orbital (FP-LMTO) method [14,15] as implemented in the RSPT code [16]. The calculations have been cross-checked within these three sets of methods providing further credence to our obtained results. Exchange and correlation effects are treated using generalized gradient approximation (GGA) [17] as well as including Hubbard U within the GGA $+ U$ framework [18]. In order to avoid any ambiguity about the choice of U and to make the GGA $+ U$ approach completely parameter free, we computed the values of effective Coulomb interaction (U) within the framework of constrained random-phase approximation (cRPA) [19] as implemented in the WIEN2K code [20]. The results of our calculations from a so-called d-d model [21] show that this method yielded a $U = 1.6$ eV and average Hund's coupling $J = 0.5$ eV for the 3d states of Cr in LaCrS$_3$. A $6 \times 12 \times 4$ k mesh has been used for the Brillouin zone (BZ) integration.

Using the converged GGA $+ U$ solutions of RSPT [16], we employed the magnetic force theorem [22,23] to extract the effective intersite exchange parameters (J_{ij}). A detailed discussion of the implementation of the magnetic force theorem in RSPT is provided in Ref. [24]. The effective J_{ij} is extracted in a linear-response manner via a Green's function technique. We have successfully used this method for other transition metal compounds [25].

III. RESULTS AND DISCUSSION

A. Magnetism and electronic structure at ambient condition

We start with the analysis of magnetic ground state and electronic structure for the bulk LaCrS$_3$ at ambient conditions using various levels of approximations in DFT such as GGA [26] and GGA $+ U$ [27]. From the experimental susceptibility data, we know that the system is antiferromagnetic in nature. To obtain an understanding of magnetism, we carried out total energy calculations for two possible magnetic states as schematically presented in Fig. 2. The results of our

TABLE I. Total energy (meV/formula unit) of the AFM state with respect to the FM state is shown for both GGA and GGA $+ U$ approaches. The magnetic moment of each Cr ion is also listed.

	GGA		GGA $+ U$	
	Energy (meV)	Moment (μ_B)	Energy (meV)	Moment (μ_B)
FM	0.00	2.90	0.00	2.90
AFM	−23.50	2.83	−14.53	2.89

calculations as demonstrated in Table I reveal that antiferromagnetic ordering between the NN Cr ions is energetically favorable which is consistent with experiment. The magnitude of this energy difference ($\Delta E = E_{FM} - E_{AFM}$) becomes slightly smaller in GGA $+ U$ scheme compared to GGA. This is not surprising as inclusion of on-site Coulomb repulsion U for the $3d$ electrons of Cr ions makes the d orbitals more localized and, as a consequence, interatomic exchange coupling is reduced. Since the value of Hubbard U for Cr-$3d$ states is estimated using cRPA, all calculations in the remainder of the paper have been carried out using the GGA $+ U$ method.

We have now analyzed the electronic structure of the antiferromagnetic state in Fig. 3. From crystal geometry, we can see that Cr atoms are surrounded by the octahedral environment formed by sulfur atoms. This leads to the splitting of d orbitals into t_{2g} and e_g states [see schematic in the inset of Fig. 3(a)]. The computed partial DOS in Fig. 3(a) shows that the Cr t_{2g} majority spin channel is fully occupied. The minority t_{2g} and e_g states appear above the Fermi level. This arrangement of d orbitals is consistent with the nominal d^3 configuration and $S = \frac{3}{2}$ spin state for Cr ions according to the Hund's rule as schematically demonstrated in the inset of Fig. 3(a). The dominant spectral weights of S-p states arise around 3 eV below the Fermi level. However, there is a small S-p spectral weight in the region where Cr majority t_{2g} states are seen, indicating a weak Cr-S hybridization due to the pi bonding between Cr-t_{2g} and S-p orbitals. Figure 3(b)

represents the band dispersion along the high symmetry directions. It reveals that a band gap of 0.5 eV appears at a Γ point and hence this system belongs to a direct-gap semiconductor. The gap is seen between the majority and t_{2g} and e_g states [Fig. 3(a)] and the origin of this gap could be attributed to the combined effects of crystal field, local exchange splitting in the Cr site, and electronic correlation of localized d states. The semiconducting ground state as predicted from our GGA $+ U$ calculations is in agreement with the experimental data [7]. From the analysis of the electronic structure, we also understood that the half filled t_{2g} (nominal d^3 configuration) states are responsible for the magnetism in this system and the computed spin moment at the Cr site turns out to be $2.89\mu_B$. Such a high value of moment again emphasizes the localized nature of the Cr-d orbitals.

In order to understand the magnetism in detail, we have computed the nature and strength of interatomic Heisenberg exchange interaction between the neighboring Cr spins by employing the magnetic force theorem [22,23]. We have estimated the strengths of a total of five interactions, where J_1, J_2, and J_4 are intrachain, while J_3 and J_5 represent the interchain coupling as marked in Fig. 1(a). The computed intersite exchange interactions corresponding to various Cr-Cr bond lengths are $J_1 = -7.5$ meV, $J_2 = 4.1$ meV, $J_3 = -0.4$ meV, $J_4 = 0.1$ meV, and $J_5 = -0.4$ meV, where negative sign indicates antiferromagnetic and positive sign corresponds to ferromagnetic coupling. We can see that the magnitude of J_1 is 1.8 times stronger than J_2. This shows a dominant antiferromagnetic exchange between the Cr ions which compliments the experimental findings of Kikkawa *et al.* [7]. The almost negligible magnitudes of J_3 and J_5 reveal that the interchain couplings along both a and c directions are very weak and the magnetism of this system could be analyzed in the form of a spin chain which proceeds along the b direction [Fig. 2(b)]. A strong antiferromagnetic J_1, relatively weaker ferromagnetic J_2, and a high value of spin moment (close to $3\mu_B$) make this an ideal candidate for the $S = \frac{3}{2}$ antiferromagnetic spin chain family of materials.
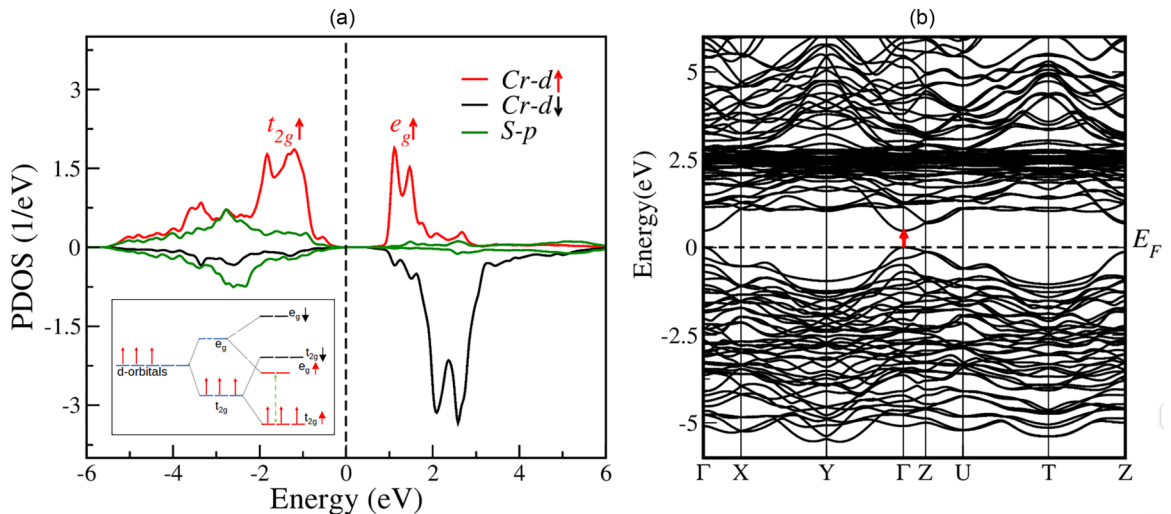

FIG. 3. (a) Computed spin-polarized partial density of states of $Cr - d$ and $S - p$ states. The Fermi energy has been set at 0 eV. In the inset, a schematic has been shown to explain the filling of d orbitals as obtained in our calculations and realization of the $S = \frac{3}{2}$ state. (b) Band dispersion of the AFM state along various high symmetry directions. The direct gap at the Γ point has been marked.

TABLE II. Orbital resolved exchange interactions at ambient conditions obtained from the converged GGA + U calculations.

J_{ij}	Bond distances (Å)	Total (meV)	$t_{2g} - t_{2g}$ (meV)	$t_{2g} - e_g$ (meV)	$e_g - e_g$ (meV)
J_1	3.41	−7.47	−13.07	6.11	−0.51
J_2	3.85	4.08	−3.87	7.75	0.20

Aiming to provide a more complete microscopic physical picture and to assess the role of different orbitals in the resulting magnetism, we will now discuss the orbital decomposed J_{ij} (i and j are two neighboring spin sites, i.e., Cr in our case) in the crystal field basis. The e_g- and t_{2g}-derived orbital contributions of dominant couplings such as J_1 and J_2 are shown in Table II. We find that, for both cases, the t_{2g}-t_{2g} couplings are antiferromagnetic, t_{2g}-e_g couplings are ferromagnetic, and e_g-e_g couplings are negligibly small. Our results also reveal that the dominating contribution for J_1 comes from t_{2g}-t_{2g} coupling, while J_2 is dominated by t_{2g}-e_g coupling. Another important point to note is that t_{2g}-t_{2g} contribution is much stronger for J_1, while t_{2g}-e_g exchanges are almost equal for J_1 and J_2. This subtle difference in orbital dependency of magnetic coupling makes the overall nature of couplings different for first and second NN Cr ions. The nature and the relative magnitude of these orbital decomposed couplings could be physically understood within the framework of the extended Kugel-Khomskii model [28,29]. In this model, each Cr-Cr exchange coupling (J_{ij}) has ferromagnetic (J_{ij}^{FM}) and antiferromagnetic (J_{ij}^{AFM}) components as described below:

$$J_{ij}^{\text{AFM}} = -4 \sum_{t_{2g}-t_{2g}} \frac{\left(t_{t_{2g}-t_{2g}}\right)^2}{U} - 4 \sum_{t_{2g}-e_g} \frac{\left(t_{t_{2g}-e_g}\right)^2}{\left(U + \Delta_{t_{2g}-e_g}\right)}, \quad (1)$$

$$J_{ij}^{\text{FM}} = 4 \sum_{t_{2g}-e_g} \frac{\left(t_{t_{2g}-e_g}\right)^2 J_H}{\left(U + \Delta_{t_{2g}-e_g} - J_H\right)\left(U + \Delta_{t_{2g}-e_g}\right)}, \quad (2)$$

$$J_{ij} = J_{ij}^{\text{AFM}} + J_{ij}^{\text{FM}}. \quad (3)$$

As evident from the above equations, the nature of the resulting interatomic magnetic interactions (J_{ij}) depends on a few parameters, namely (a) crystal-field splitting ($\Delta_{t_{2g}-e_g}$), (b) effective virtual hopping strengths between the relevant orbitals ($t_{2g} - t_{2g}$, $t_{2g} - e_g$), (c) the nominal fillings of those orbitals, and (d) Hund's coupling strength (J_H), as well as the magnitude of Hubbard U of correlated d states. In our case, the relevant orbital for magnetism is half filled Cr-t_{2g} states and the empty e_g states appear slightly above them due to the octahedral crystal field. The hopping being spin conserved, up-spin electrons of a Cr^{3+} are allowed to hop to the neighboring Cr site if the up-spin channel of that site is partially or fully empty. Since t_{2g} states are exactly half filled, intersite t_{2g}-t_{2g} virtual hoppings are allowed only if they possess antiparallel alignments [see schematic in Figs. 4(a) and 4(b)], making the t_{2g}-t_{2g} exchange completely antiferromagnetic in nature and it has no contribution in J_{ij}^{FM} as seen in Eq. (2). Since both the spin channels of e_g states are empty, virtual intersite t_{2g}-e_g hoppings are allowed for both parallel and antiparallel alignments [see schematic in Figs. 4(c) and 4(d)]. However, the parallel alignment is energetically favored because of the Hund's coupling and thus we see a ferromagnetic t_{2g}-e_g coupling in our calculations. The magnitude of

these couplings will primarily depend on the t_{2g}-t_{2g} and t_{2g}-e_g hopping strengths in an effective low energy Hamiltonian for d states where the S-p states are downfolded. In this picture, e_g-e_g interaction should be zero. A small value obtained in our calculations arises due to the distortion in the octahedra, resulting in slight mixing of t_{2g} and e_g states. Thus we provided the microscopic mechanism behind the nature of the orbital resolved couplings which appears a crucial quantity for explaining the resulting opposite sign of J_1 and J_2, despite their similar bond distances. We believe that this mechanism is generic and should be useful in understanding the magnetism of other transition metal (TM) compounds where TM possesses a nominal d^3 configuration (half filled t_{2g}).

Next, we analyze the effect of relativistic spin-orbit coupling (SOC) which is known to play a crucial role in realizing novel exotic phases in many real materials. In the absence of SOC, the exchange interactions are isotropic with spin rotational invariance. However, SOC may lower the symmetry and gives rise to anisotropic interactions as theoretically explained by Moriya in Ref. [30] by extending the Anderson superexchange theory [31]. The presence of spin-orbit coupling, leading to a sizable magnetocrystalline anisotropy (MAE), Dzyaloshinskii-Moriya (DM) interactions, and symmetric anisotropic interactions has recently been studied in Cr-based layered compounds such as CrX_3 (X = Cl, Br, I), $CrGeTe_3$ etc. The MAE helps to overcome thermal fluctuations and gives rise to long-range magnetic ordering in low-dimensional spin systems. On the other hand, sizable DM interactions often compete with the Heisenberg J_{ij} and give rise to topologically nontrivial spin textures. We first estimated MAE by computing the energies corresponding to different spin quantization axes within the GGA + U
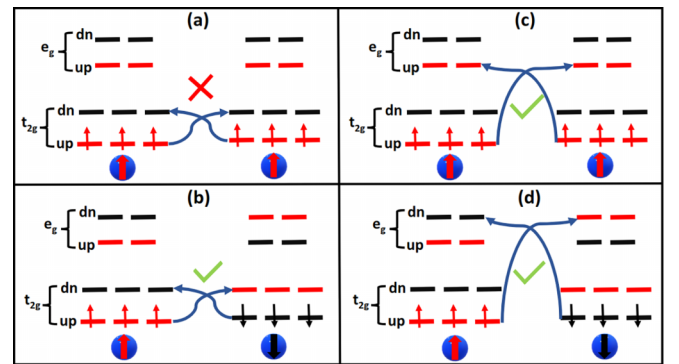

FIG. 4. Hopping being spin-conserved, the schematic demonstrates that intersite hopping between t_{2g} states are (a) forbidden when Cr ions are ferromagnetically aligned and (b) allowed when they are antiferromagnetically aligned. Similarly (c), (d) t_{2g}-e_g intersite hopping is allowed for both kinds of coupling. However, ferromagnetic coupling is energetically favored due to Hund's coupling.

TABLE III. Total energy, spin moments, and orbital moments of Cr ions for a given magnetization direction obtained from GGA + U + SOC calculations. The energies are relative to the energy of the cell with the magnetization along the b axis.

	b axis		a axis		c axis	
	Energy (meV)	Moment (μ_B)	Energy (meV)	Moment (μ_B)	Energy (meV)	Moment (μ_B)
GGA + U + SOC	0.00	2.89 (0.02)	−0.38	2.89 (0.04)	−0.25	2.89 (0.03)

approach incorporating SOC. The computed energies (Table III) reveal that the crystallographic a axis is the easy axis of magnetization (lowest energy). The spin moment on the Cr site is the same for all quantization axes as expected and the orbital moment is $0.04\mu_B$ for the easy axis of magnetization. The MAE is defined as the energy difference between the easy and hard axis of magnetization. The computed value of MAE = $E_{100} - E_{010} = -0.38$ meV. Interestingly the magnetic moment favors aligning perpendicularly to the direction of the spin chain. The magnitude of the spin, orbital moments, and MAE in LaCrS$_3$ compare well with other reported Cr-based compounds such as CrI$_3$ [32], where the computed orbital moment and MAE are $0.07\mu_B$ and 0.3 meV, respectively. It is worthwhile to note here that, despite having a small orbital moment, the effective SOC is strong in this compound as revealed from the large MAE. This could be attributed to the large spin moment on the Cr site and the highly anisotropic crystal environment of this material, which are essential requirements to exhibit large MAE in bulk materials. In a few previous studies on Cr-based compounds [33,34], it has been claimed SOC is not directly contributed by the magnetic ion alone but induced by the nonmagnetic ligand states. For instance, MAE is shown to arise due to the SOC of iodine ions [33,34] and Te ions, respectively [34], for CrI$_3$ and CrGeTe$_3$. In order to investigate this possibility, we have computed the site decomposed MAE as a function of SOC strength. The contributions of La, Cr, and S atoms to the total MAE are separately displayed in Fig. 5. Contrary to the previous reports [33,34], we found that contribution of La and S are negligibly small so that the dominant contribution comes from the magnetic Cr ions.

Since the effective SOC is found significantly large and comparable with other Cr based materials, we further mapped the computed energies from GGA + U + SOC onto a generalized Heisenberg model as given below:

$$H = \sum_{i \neq j} e_i^\alpha J_{ij}^{\alpha\beta} e_j^\beta, \quad \alpha, \beta = x, y, z. \tag{4}$$

Here the magnetic exchange parameter J_{ij} is a 3×3 tensor for the fully relativistic case and α, β represent tensor components along x, y, and z axis. We calculated all its components to estimate the DM interaction vector (D_{ij}) (antisymmetric anisotropic interaction) and symmetric anisotropic interaction (C_{ij}), which are given by

$$D_{ij}^x = \tfrac{1}{2}\{J_{ij}^{yz} - J_{ij}^{zy}\}, \quad D_{ij}^y = \tfrac{1}{2}\{J_{ij}^{xz} - J_{ij}^{zx}\},$$
$$D_{ij}^z = \tfrac{1}{2}\{J_{ij}^{xy} - J_{ij}^{yx}\}, \tag{5}$$

$$C_{ij}^x = \tfrac{1}{2}\{J_{ij}^{yz} + J_{ij}^{zy}\}, \quad C_{ij}^y = \tfrac{1}{2}\{J_{ij}^{xz} + J_{ij}^{zx}\},$$
$$C_{ij}^z = \tfrac{1}{2}\{J_{ij}^{xy} + J_{ij}^{yx}\}. \tag{6}$$

A detailed discussion on the implementation and calculations of these parameters is given in Refs. [35,36]. As shown in Table IV, the DM interaction for the first NN is zero due to the presence of space-inversion symmetry. However, the second NN interactions are relatively strong and the DM vector lies in the x-z plane, which is perpendicular to the direction of the chain (y axis). The magnitude of C_{ij} is found to be very small for both the neighbors. Based on these interactions, we computed the spin-wave dispersions (see Fig. 6) using linear spin-wave theory as implemented in the SPIN-W code [37]. There are two Cr atoms which form the double chain in this system, resulting in two bands in the magnetic excitation spectrum. When anisotropic components of magnetic interactions are not considered, the spin wave dispersions are degenerate and the degeneracy is lifted after including DM interactions in the spin Hamiltonian (see inset of Fig. 6). These results can be helpful for future neutron scattering experiments and analysis. We find that the magnetic propagation vector $\nu = (0\,0\,0)$ comes out to be lowest in energy and the second nearest neighbor DM interaction does not yield any spin canting in this system. We note that the nature of our
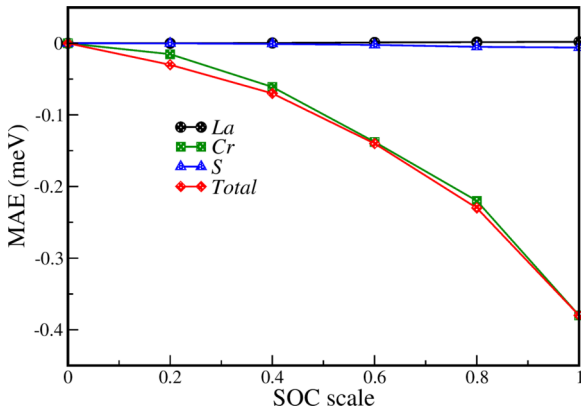

FIG. 5. Contributions of La, Cr, and S atoms to the magnetocrystalline anisotropy as a function of SOC strength. Note that the value of 1.0 represents the SOC strength that corresponds to the actual strength and 0 implies that there is no SOC.

TABLE IV. Three components of DM interactions vector and anisotropic symmetric exchange between first and second NN Cr ions as obtained from GGA + U + SOC calculations.

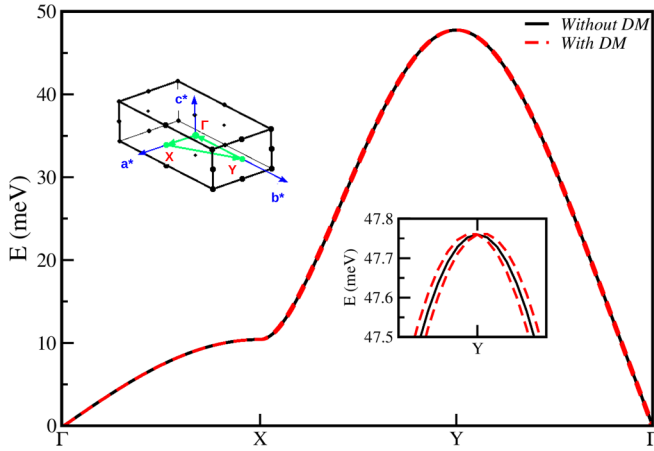| Site	Distance (Å)	D_x	D_y	D_z	C_x	C_y	C_z
First NN	3.41	0.00	0.00	0.00	−0.002	0.002	0.006
Second NN	3.85	0.05	0.00	−0.08	0.00	−0.004	0.00

FIG. 6. Spin-wave dispersions along high-symmetry directions in the BZ computed with and without including DM interactions. The inset shows the BZ and the labels of high-symmetry k points. The inset also displays the spin-wave dispersions around the Y point within a smaller energy window to portray the degeneracy breaking due to the presence of DM interaction.
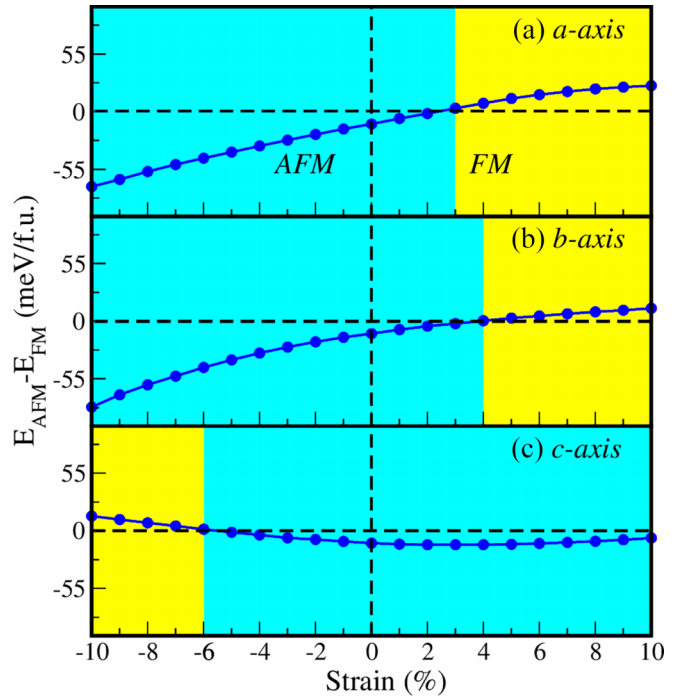

FIG. 7. Energy difference between FM and AFM states as a function of strain along the (a) a, (b) b, and (c) c axis is displayed. The magnetic transition is highlighted.

computed spin-wave spectrum agrees well with the other spin-chain antiferromagnets such as RbFeS$_2$ [38].

B. Magnetic and electronic transition under uniaxial strain

The strain engineering is considered to be a promising route for realizing electronic and magnetic transition in transition metal compounds [39]. To explore possibilities like antiferromagnetic to ferromagnetic transition, tuning the effective SOC, switching the direction of the easy/hard axis of magnetization, tuning the nature and magnitude of band gap, etc., we have studied the magnetism and electronic structure of LaCrS$_3$ under the application of tensile and compressive strain along all the three crystallographic directions. The strain is defined as follows: $\nu = \frac{l-l_0}{l_0}$, where l_0 and l are pristine and strained lattice constants, respectively. Thus the compressive strain corresponds to the negative values and positive values representing tensile strain. The value of l_0 has been taken from the experimentally reported lattice parameters [7] and ionic relaxation has been performed for every value of ν.

Lowest energy magnetic state. We have computed total energies corresponding to the FM (E_{FM}) and AFM state (E_{AFM}) by applying uniaxial strain along all the three directions and the energy difference $\delta E = E_{AFM} - E_{FM}$ presented in Figs. 7(a)–7(c). We found that due to compressive strain along the a and b axis, δE increases monotonously along the negative direction, indicating stronger stability for the AFM state. However, δE becomes zero at about 2% of tensile strain and moves towards positive values upon enhancing the tensile strain. Thus our results reveal a magnetic transition from AFM state to FM state just by applying 2% of tensile strain. However, the change of δE is much smaller when the strain is applied along the c direction. This is not surprising considering the fact that Cr ions are located in the $a - b$ plane and well separated along the c directions (fifth NN). Hence all the remaining discussions are focused on the strain along a and b directions.

Microscopic origin of magnetic transition. In order to understand the origin of magnetic transition, we computed the dominant magnetic exchange interactions (J_1, J_2) and their orbital decomposition as a function of external uniaxial strain. The changing trend of both couplings for strain along a and b axes are displayed in Figs. 8(a) and 8(b), respectively. The results show that the compressive strain region is strongly dominated by antiferromagnetic J_1, while in the tensile regions, J_1 and J_2 have comparable magnitudes. A critical value of tensile strain is able to make the net coupling ($J_{tot} = J_1 + J_2$) positive, giving rise to the occurrence of magnetic transition as discussed above. Our primary observations can be summarized as follows: (i) the first nearest neighbor exchange coupling (J_1) strongly varies under the application of strain along both axes (a and b), (ii) the influence of strain on the second NN coupling J_2 is minimal, (iii) the orbital resolved exchange couplings for both uniaxial strain reveal that t_{2g}-t_{2g} coupling is responsible for the strong variation of J_1, while t_{2g}-e_g coupling does not vary significantly as a function of strain, (iv) in the case of J_2, the ferromagnetic component, t_{2g}-e_g coupling always remains slightly stronger than antiferromagnetic t_{2g}-t_{2g} coupling and their magnitudes are small, making the net coupling weakly ferromagnetic, and (v) interestingly in the entire region of our study, the nature of t_{2g}-t_{2g} coupling remains antiferromagnetic and t_{2g}-e_g is ferromagnetic, which is consistent with the Kugel-Khomskii model as discussed before [see Eqs. (1) and (2) and the corresponding analysis]. Thus our results explain the microscopic origin of the strongly antiferromagnetic spin chain region under the influence of compressive strain and the relatively weaker ferromagnetic spin chain region after a critical value of tensile strain. We also note that, at higher values of compression, J_1
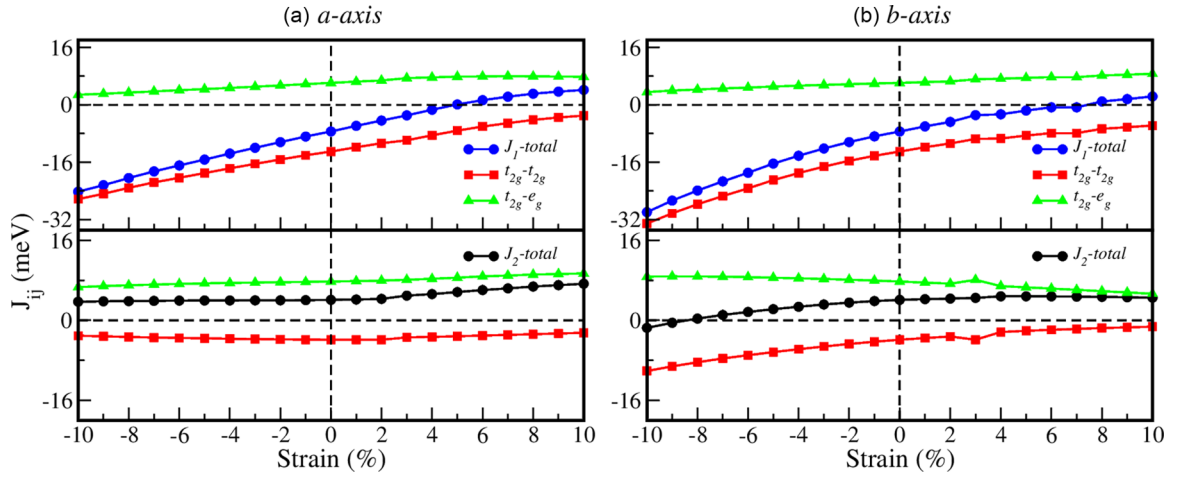
FIG. 8. Variations of orbital resolved contributions (t_{2g}-t_{2g} and t_{2g}-e_g) to the total J_1 and J_2 as a function of strain along the (a) a and (b) b axis are displayed.

is significantly stronger than J_2 and hence the system will behave like a uniform antiferromagnetic spin chain compound.

Effect of strain on electronic structure. To understand the effect of strain on the electronic properties, we computed the band gap for various values of strain along the a and b axes. The results are displayed in Figs. 9(a) and 9(b), which illustrate that the system remains insulating even after the magnetic transition to FM state under the influence of tensile strain. However, the band gap shrinks compared to the ambient condition. Most interestingly, we could realize a FM insulating state in the tensile region. On the other hand, we observe a monotonic reduction of band gap as compressive strain enhances and, at −9% strain along the b axis, it becomes zero. The calculated total DOS for strain along the a and b axes are displayed in Figs. 9(c) and 9(d), respectively. These results indicate that the valence band does not significantly change due to strain, while the conduction band arising from Cr-d states broadens due to compression and a small spectral weight at the Fermi level is observed for −10% strain along the b axis [see inset of Fig. 9(d)]. The band dispersion along the high-symmetry paths of the Brillouin zone at the critical value of strain (−9%) is displayed in Fig. 9(e). Remarkably

the band dispersion has a very interesting character that the valence band and conduction band edge touch each other near the Γ point and the gap still persists at all other points. These results indicate that compressed LaCrS$_3$ exhibits a gapless semiconducting antiferromagnetic ground state which has potential applications in spintronic devices [40–42]. The gapless semiconductor is a very interesting class of materials where threshold energy is not required to move electrons from valence to conduction band and thus the electron mobility is much higher than the usual semiconductors. The most famous example in this category is graphene which has gapless band structure and linear energy-momentum dispersion [43]. There are a few other examples also such as PbPdO$_2$ [42] and VTaNbAl [44]. However, none of these materials are antiferromagnetic. The antiferromagnetism along with gapless electronic structure is truly rare. Thus our results provide a route to obtain such a ground state in a transition metal compound.

C. Stability analysis

To account for the stability of the system under compressive and tensile strain, we have calculated the phonon
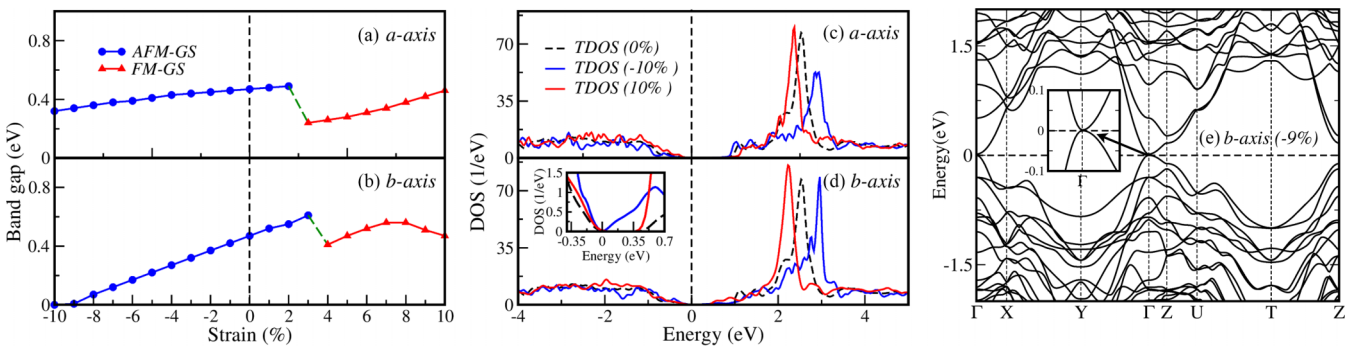

FIG. 9. Variation of the band gap in the AFM and FM ground state (GS) as a function of strain along the (a) a and (b) b axis. The total DOS in their respective magnetic ground state for three values of strains (+10%, 0%, and −10%) along the (c) a and (d) b axis. The inset in (d) shows TDOS in the close vicinity of Fermi energy to portray a vanishing energy gap at −10%. (e) The band dispersion at the critical value of strain along the b axis (−9%) where the band gap becomes zero. It clearly displays the realization of an interesting nongap semiconducting state where the band gap is zero only at the center of the BZ (Γ point). The inset demonstrates the dispersion at and around the Γ point.
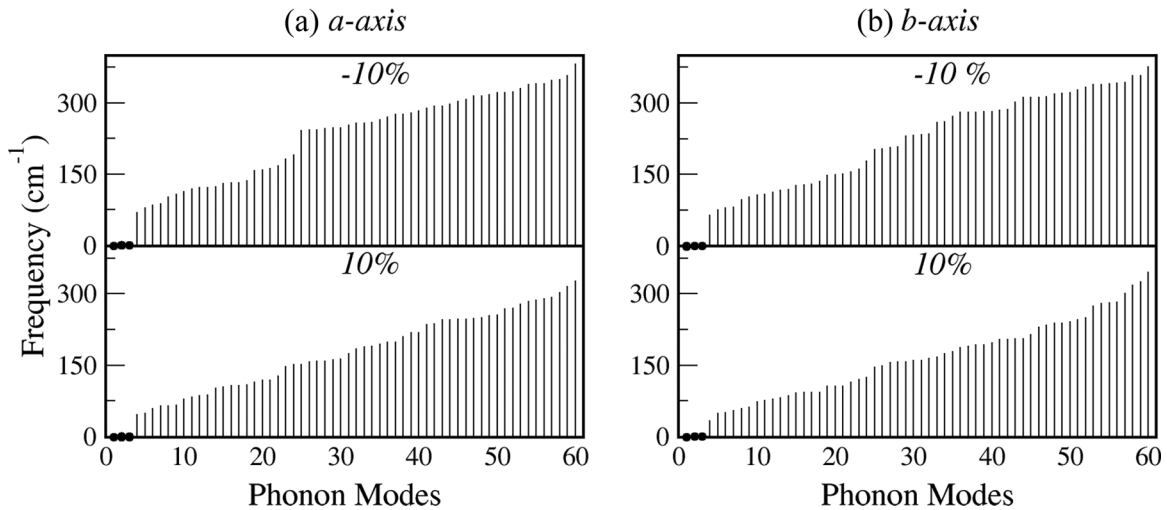
FIG. 10. Phonon frequencies (in cm^{-1}) at the Γ point of the Brillouin zone under (a) compressive strain and (b) tensile strain. The mode numbers from 1 to 60 (total 60 modes corresponding to 20 atoms in the unit cell) are displayed in the x axis and the bar in the y axis denotes the corresponding frequency. We note that the first few frequencies are very small for all cases.

frequencies at the Γ point of the Brillouin zone from the converged GGA $+ U$ solutions. The finite difference method as implemented in VASP code has been employed. In this approach, the second order derivative of the total energy with respect to ionic displacements, i.e., the force constants or Hessian matrix, are calculated using finite differences. The dynamical matrix is thus constructed from force constants and diagonalized to obtain frequencies corresponding to each phonon mode. The calculated phonon frequencies under strain along a and b axes are shown in Figs. 10(a) and 10(b), respectively. It can be seen that there are total 60 frequencies corresponding to the 20 atoms in the unit cell. Our results find that all the modes under 10% compression and stretch are positive. Since there are no imaginary frequencies, the system is considered to be stable under strain.

IV. CONCLUSION

In conclusion, we studied the electronic and magnetic properties of LaCrS$_3$ using first-principles DFT $+ U$ calculations where Hubbard U was estimated from the cRPA method. We found that the system is antiferromagnetic and semiconducting with a direct band gap of 0.5 eV at ambient condition. Our computed exchange interactions based on the magnetic force theorem reveal that Cr spins form a nonfrustrated chain network which propagates along the crystallographic b axis. Within this chain, the first NN interaction is found to be strongly antiferromagnetic, while the second NN is weakly ferromagnetic. We showed that the contradictory nature of these interatomic (Cr-Cr) magnetic interactions despite very similar bond distances could be understood based on orbital resolved components in a crystal-field basis. Our calculations demonstrate that the SOC effect is significant, leading to sizable values of MAE and DM interactions. The strengths of these quantities are comparable with other Cr-based compounds such as CrI$_3$. Further, we applied mechanical strain along the a and b axes and found that the system exhibits magnetic transition to an insulating FM ground state due to tensile strain. On the other side, the compressive strain given is able to strongly enhance the first NN interaction, giving rise to a uniform antiferromagnetic spin chain behavior in LaCrS$_3$. Interestingly a gapless AFM ground state could be also realized for -9% strain along the b axis, where the valence band and conduction just touch each other near the Γ point and all the other parts of the BZ are gapped. Thus, under the application of strain, we report two interesting transitions, namely AFM to FM transition and normal semiconductor to a gapless semiconductor transition in LaCrS$_3$. The realization of such a gapless semiconducting state in LaCrS$_3$ opens up huge possibilities for industrial applications in making new spintronic devices.

[1] *Introduction to Frustrated Magnetism*, edited by C. Lacroix, P. Mendels, and F. Mila (Springer, Berlin, 2011).

[2] F. D. M. Haldane, Phys. Rev. Lett. **50**, 1153 (1983).

[3] M. Kenzelmann, R. A. Cowley, W. J. L. Buyers, Z. Tun, R. Coldea, and M. Enderle, Phys. Rev. B **66**, 024407 (2002).

[4] K. S. Burch, D. Mandrus, and J.-G. Park, Nature (London) **563**, 47 (2018).

[5] H. Wang, V. Eyert, and U. Schwingenschlögl, J. Phys.: Condens. Matter **23**, 116003 (2011).

[6] J. Shang, X. Tang, X. Tan, A. Du, T. Liao, S. C. Smith, Y. Gu, C. Li, and L. Kou, ACS Appl. Nano Mater. **3**, 1282 (2020).

[7] S. Kikkawa, Y. Fujii, Y. Miyamoto, F. Kanamaru, A. Meerschaut, A. Lafond, and J. Rouxel, J. Solid State Chem. **139**, 233 (1998).

[8] X. Obradors, J. Bassas, J. Rodriguez, J. Pannetier, A. Labarta, J. Tejeda, and F. Berry, J. Phys.: Condens. Matter **2**, 6801 (1990).

[9] A. Qaiumzadeh, L. A. Kristiansen, and A. Brataas, Phys. Rev. B **97**, 020402(R) (2018).

[10] G. Kresse and J. Hafner, Phys. Rev. B **47**, 558 (1993).

[11] G. Kresse and J. Furthmüller, Phys. Rev. B **54**, 11169 (1996).

[12] P. E. Blöchl, Phys. Rev. B **50**, 17953 (1994).

[13] K. Schwarz and P. Blaha, Comput. Mater. Sci. **28**, 259 (2003).

[14] O. K. Andersen, Phys. Rev. B **12**, 3060 (1975).

[15] J. M. Wills and B. R. Cooper, Phys. Rev. B **36**, 3809 (1987).

[16] J. M. Wills, O. Eriksson, M. Alouni, and D. L. Price, *Electronic Structure and Physical Properties of Solids: The Uses of the LMTO Method* (Springer-Verlag, Berlin, 2000).

[17] J. P. Perdew, K. Burke, and M. Ernzerhof, Phys. Rev. Lett. **77**, 3865 (1996).

[18] A. I. Liechtenstein, V. I. Anisimov, and J. Zaanen, Phys. Rev. B **52**, R5467 (1995).

[19] F. Aryasetiawan, M. Imada, A. Georges, G. Kotliar, S. Biermann, and A. I. Lichtenstein, Phys. Rev. B **70**, 195104 (2004).

[20] L. Vaugier, H. Jiang, and S. Biermann, Phys. Rev. B **86**, 165105 (2012).

[21] S. K. Panda, B. Pal, S. Mandal, M. Gorgoi, S. Das, I. Sarkar, W. Drube, W. Sun, I. Di Marco, A. Lindblad, P. Thunström, A. Delin, O. Karis, Y. O. Kvashnin, M. van Schilfgaarde, O. Eriksson, and D. D. Sarma, Phys. Rev. B **93**, 235138 (2016).

[22] A. Liechtenstein, M. Katsnelson, V. Antropov, and V. Gubanov, J. Magn. Magn. Mater. **67**, 65 (1987).

[23] M. I. Katsnelson and A. I. Lichtenstein, Phys. Rev. B **61**, 8906 (2000).

[24] Y. O. Kvashnin, O. Grånäs, I. Di Marco, M. I. Katsnelson, A. I. Lichtenstein, and O. Eriksson, Phys. Rev. B **91**, 125133 (2015).

[25] S. K. Panda, Y. O. Kvashnin, B. Sanyal, I. Dasgupta, and O. Eriksson, Phys. Rev. B **94**, 064427 (2016).

[26] D. C. Langreth and J. P. Perdew, Phys. Rev. B **21**, 5469 (1980).

[27] V. I. Anisimov, J. Zaanen, and O. K. Andersen, Phys. Rev. B **44**, 943 (1991).

[28] K. I. Kugel and D. I. Khomskii, Zh. Eksp. Teor. Fiz. **64**, 1429 (1973) [Sov. Phys. JETP **37**, 725 (1973)].

[29] K. I. Kugel and D. I. Khomskii, Sov. Phys. Usp. **25**, 231 (1982).

[30] T. Moriya, Phys. Rev. **120**, 91 (1960).

[31] P. W. Anderson, Phys. Rev. **115**, 2 (1959).

[32] S. Bandyopadhyay, F. L. Buessen, R. Das, F. G. Utermohlen, N. Trivedi, A. Paramekanti, and I. Dasgupta, Phys. Rev. B **105**, 184430 (2022).

[33] J. L. Lado and J. Fernández-Rossier, 2D Mater. **4**, 035002 (2017).

[34] C. Xu, J. Feng, H. Xiang, and L. Bellaiche, npj Comput. Mater. **4**, 57 (2018).

[35] Y. O. Kvashnin, A. Bergman, A. I. Lichtenstein, and M. I. Katsnelson, Phys. Rev. B **102**, 115162 (2020).

[36] V. Borisov, Y. O. Kvashnin, N. Ntallis, D. Thonig, P. Thunström, M. Pereiro, A. Bergman, E. Sjöqvist, A. Delin, L. Nordström, and O. Eriksson, Phys. Rev. B **103**, 174422 (2021).

[37] S. Toth and B. Lake, J. Phys.: Condens. Matter **27**, 166002 (2015).

[38] L. Li, L. Zheng, B. A. Frandsen, A. D. Christianson, D.-X. Yao, M. Wang, and R. J. Birgeneau, Phys. Rev. B **104**, 224419 (2021).

[39] A. C. Garcia-Castro, A. H. Romero, and E. Bousquet, Phys. Rev. Lett. **116**, 117202 (2016).

[40] I. M. Tsidilkovsk, *Electron Spectrum of Gapless Semiconductors*, Springer Series in Solid-State Sciences (Springer Berlin, Heidelberg, 1996).

[41] X.-L. Wang, S. X. Dou, and C. Zhang, NPG Asia Mater. **2**, 31 (2010).

[42] X. L. Wang, Phys. Rev. Lett. **100**, 156404 (2008).

[43] A. H. Castro Neto, F. Guinea, N. M. R. Peres, K. S. Novoselov, and A. K. Geim, Rev. Mod. Phys. **81**, 109 (2009).

[44] D. Rani, P. C. Sreeparvathy, K. G. Suresh, R. Chatterjee, and A. Alam, Phys. Rev. B **107**, 134434 (2023).